Environmental Map Building and Moving Object Tracking Using Helmet-Mounted LiDAR and IMU for Micromobility

Ibuki Yoshida, Akihiko Yoshida
Graduate School of Science and Engineering
Doshisha University
Kyotanabe, Japan
e-mail: {ctwh0151, ctwj0112}@mail4.doshisha.ac.jp

Masafumi Hashimoto, Kazuhiko Takahashi
Faculty of Science and Engineering
Doshisha University
Kyotanabe, Japan
e-mail: {mhashimo, katakaha}@mail.doshisha.ac.jp

Abstract— **This paper presents a method of environmental map building and moving object tracking using Light Detection And Ranging (LiDAR) and Inertial Measurement Unit (IMU) mounted on a smart helmet worn by a micromobility rider. This presented method can be used for active safety for micromobility, such as bicycles, e-bikes, and electric scooters. Distortion in scan data from LiDAR is corrected by estimating the helmet pose (three-dimensional (3D) position and attitude angle) based on information obtained from normal distributions transform scan matching and IMU. The corrected LiDAR scan data are classified into scan data on road surfaces, road boundaries, stationary objects, and moving objects in the environments. Moving object scan data are used for moving object tracking. Stationary object and road boundary scan data are used to represent 3D stationary objects and road obstacles, such as curbs, gutters, and steps. Road surface scan data from LiDAR are in conjunction with IMU acceleration, and small road unevenness, such as potholes and humps, is detected to reduce the falling risk of micromobility. Furthermore, road surface conditions are identified by integrating IMU acceleration data, and a road surface condition map is constructed to provide safety and comfortability for micromobility riders in environments. Experiments conducted on a road on our university campus demonstrate the effectiveness of the proposed method.**

Keywords-helmet LiDAR/IMU; micromobility; environmental map building; moving object tracking; road boundary detection; road unevenness detection; road surface condition estimation.

I. INTRODUCTION

This paper is an extended and improved version of an earlier paper presented at the IARIA Conference on Sensor Device Technologies and Applications (SENSORDEVICES 2022) [1] in Lisbon.

Numerous studies on active safety and autonomous driving in the field of Intelligent Transportation Systems (ITS) have been conducted [2]. In the field of last-mile automation, there has also been flourishing study on delivery robots [3]. The environmental map building [4, 5] and tracking of moving objects, such as cars, cyclists and pedestrians [6, 7], are important issues for autonomous driving and the active safety of vehicles and mobility robots. Many related studies have been conducted using cameras, radars, and Light Detection And Ranging (LiDAR) [8, 9]. In this paper, we focus on environmental map building and moving object tracking with vehicle-mounted LiDAR.

To reduce carbon emissions and resolve congestion, the use of single-seater micromobility, such as bicycles, e-bikes, electric scooters, and standing-type personal mobilities, has been attracting attention as a means of short-distance transportation in urban cities [10]. The coronavirus disease 2019 has made people highly resistant to using conventional means of urban transportation, such as crowded trains and buses. Therefore, micromobilities have become more prevalent as a means of reducing the risk of infection in future endemic societies.

Micromobilities can be driven on a road, a bicycle lane, or a section of sidewalk. In addition, micromobilities are prone to tipping over due to unevenness in road surfaces, and there is also the issue that pedestrians in the vicinity who are "doing something while walking" will not notice the approach of micromobilities.

Although the frequency of traffic accidents involving micromobility has increased recently, study on active safety for micromobility is far behind. As a result, this paper explores environmental sensing for micromobility, such as environmental map building and moving object recognition for active safety for micromobility.

In the case of micromobility systems, it is difficult to mount many sensors on the vehicle body, as is the case with cars, because of size and theft concerns. Thus, it is desirable to mount small and easily detachable sensors on the handlebar of a micromobility or the helmet worn by the micromobility rider. This paper presents a Helmet-Mounted LiDAR (HML)-based environmental map building and the tracking of moving objects, such as cars, two-wheelers, and pedestrians, in dynamic and Global Navigation Satellite System (GNSS)-denied environments. Moving object tracking and map building related to stationary 3D objects and road obstacles, such as curbs, gutters, and steps, are essential for preventing collision accidents of micromobilities.

The detection of small road unevenness, such as potholes and humps, as well as the estimation of road surface conditions, is also required to prevent the falling risk of micromobility and improve rider comfort. However, it is difficult to detect small road unevenness and estimate road surface conditions using only LiDAR scan data. In this paper, these are performed using acceleration information from a helmet-mounted Inertial Measurement Unit (IMU).

The rest of this paper is organized as follows. Section II presents an overview of related work, and Section III describes the experimental system. Section IV overviews the

experimental map building and moving object tracking. Section V explains the estimation method of the helmet self-pose and the distortion-correction method of LiDAR scan data, and Section VI presents the method for classifying LiDAR scan data into scan data on road surfaces, road boundaries, stationary objects, and moving objects. Section VII presents the method for estimating the road boundaries and tracking moving objects, and Section VIII presents the method for detecting small road unevenness and estimating road surface conditions using IMU acceleration. Section IX presents experimental results to verify the proposed method, followed by the conclusions and future works in Section X.

II. RELATED WORK

Many studies on environmental mapping and moving object tracking have been conducted [4–7]. We previously presented an environmental map-building method using car and motorcycle-mounted LiDAR based on Normal Distributions Transform (NDT)-Graph Simultaneous Localization And Mapping (SLAM) [11, 12] to build a three-dimensional (3D) point cloud map in community road environments. We also presented a method of moving object tracking using car and motorcycle-mounted LiDAR [13, 14].

Recently, we proposed a method of building a 3D point-cloud map in sidewalk and roadway environments using LiDAR attached to the rider's helmet (HML) of a micromobility [15]. This study is an extension of our previous works [14, 15] on environmental map building using HML and moving object tracking by motorcycle-mounted LiDAR, and these methods are integrated into our HML system.

Several studies have been conducted on surrounding environmental sensing using HML. Indoor SLAM, where people on helmets equipped with two-dimensional (2D) or one-dimensional (1D) LiDAR walk around in building and factory environments, has been reported [16–18]. Niforatos et al. [19] presented a method of skier detection using 1D LiDAR attached to ski helmets to reduce the risk of accidents on ski slopes.

Apart from map building and moving object tracking, many studies on road surface condition estimation have been proposed using car and bicycle-mounted sensors, such as LiDAR, accelerometer, and smartphone sensors [20–24]. However, the estimation of road surface conditions using a helmet-mounted IMU remains a challenge.

To the best of our knowledge, no studies have been conducted on environmental sensing including environmental map building and moving object tracking in sidewalks and roadways using 3D LiDAR and an IMU attached to the rider helmet of a micromobility. Although there have been several studies on helmets with sensors (smart helmets) in the ITS field [25], their use is limited to alcohol detection in motorcycle riders and collision-accident detection, as well as confirming rider safety after accidents.

III. EXPERIMENTAL SYSTEM

Figure 1 shows an overview of the smart helmet. The upper part of the helmet is equipped with a mechanical 64-layer LiDAR (Ouster, OS0-64) and an IMU (Xsens, MTi-300).

The HML has a maximum range of 55 m, a horizontal field of view of 360° with a resolution of 0.35°, and a vertical field of view of 90° with a resolution of 1.4°. LiDAR can obtain 1024

measurements (distance, direction, and reflected light intensity) every 1.56 ms (every 5.6° in the horizontal direction). Therefore, approximately 66,000 scan data points are acquired in one rotation (360° observation) period (100 ms).

The attitude angle (roll and pitch angles), angular velocity (roll, pitch, and yaw angular velocities), and three-axis acceleration of the helmet are obtained from the IMU every 10 ms. The measurement error for the attitude angle is less than ± 0.3°, that of the angular velocity is less than ± 0.2°/s, and that of the acceleration is less than ± 5 mG.

The weight of the mechanical LiDAR is 0.5 kg, and the smart helmet is heavier and larger than usual helmets. Therefore, the LiDAR reduces the usability and practicability of the smart helmet. Moreover, it affects the performance of the helmet in the event of a crash. However, modern LiDAR technology [26] has been developing smaller, more lightweight, and lower power consumption solid-state LiDARs than mechanical LiDARs. The use of solid-state LiDARs will significantly improve the usability and practicability of smart helmets.

IV. OVERVIEW OF ENVIRONMENTAL MAP BUILDING AND MOVING OBJECT TRACKING

Figure 2 shows the sequence of environmental map building and moving object tracking. LiDAR scan data captured in the helmet coordinate system attached to the HML are mapped onto the world coordinate system using the self-pose (3D position and attitude angle) information of the helmet. For this, an accurate self-pose of the helmet is required. NDT scan matching [27] is employed to estimate the self-pose in GNSS-denied environments.

Because LiDAR scans lasers in the omnidirection, all scan data within one scan cannot be obtained at a single location when the micromobility is moving or swinging, or when the rider's body is swinging. Therefore, if all scan data within one scan is transformed using the pose information of the helmet simultaneously, distortion arises in the LiDAR scan data mapped in the world coordinate system. Because distortion leads to inaccurate results in map building and moving object tracking, distortion correction of the LiDAR scan data is required. The distortion-correction method [15] is briefly described in Section V.

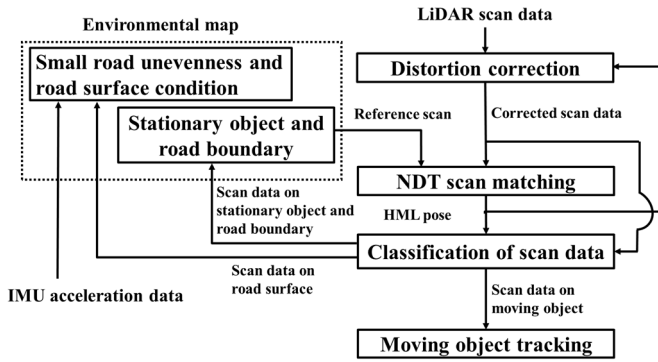Figure 1. Overview of the experimental smart helmet.

Figure 2. Sequence of environmental map building and moving object tracking.

The distortion-corrected LiDAR scan data are classified into scan data on road surfaces, road boundaries, stationary objects, and moving objects. Scan data on road surfaces (referred to as road surface scan data) are used to recognize areas where micromobility can travel. Scan data on stationary objects in the environment (stationary object scan data) are used to build a stationary object map. Scan data on moving objects (moving object scan data) are used for moving object tracking. Scan data relating to road boundaries (road boundary scan data) are used to detect road obstacles, such as fallen objects on the road, and boundaries of the road, e.g., grooves and curbs. The classification method of road surface, road boundary, stationary object, and moving object scan data from entire LiDAR scan data is described in Section VI. The methods for accurately estimating road boundaries from road boundary scan data and for accurately tracking moving objects from moving object scan data are explained in Section VII.

Although the position determination of small unevenness on road surfaces, such as potholes, cracks, and manhole covers, is necessary for preventing fall accidents from micromobilities, it is difficult to detect them with only LiDAR. Therefore, such small road unevenness is detected using acceleration data from IMU. Furthermore, the road surface condition is estimated using IMU acceleration data, and the related map is built to predict the safety of micromobility and the comfort of the rider. These methods are described in Section VIII.

Maps for stationary objects, road boundaries, and road unevenness, as well as moving object tracking, are built recursively after each LiDAR scan data and IMU acceleration data are obtained, whereas maps for road surface conditions are built in batch after a micromobility run is complete.

V. SELF-POSE OF HELMET AND DISTORTION CORRECTION OF LiDAR SCAN DATA

This section briefly explains the self-pose (position and attitude angle) estimation of the helmet using NDT scan matching and Extended Kalman Filter (EKF)-based distortion correction of LiDAR scan data.

A. Estimation of Helmet Self-Pose

For the i-th measurement point ($i = 1, 2, …n$) in the LiDAR scan data, the position in the helmet coordinate system is denoted by $\boldsymbol{p}_{Hi} = (x_{Hi}, y_{Hi}, z_{Hi})^T$, and that in the world coordinate system by $\boldsymbol{p}_i = (x_i, y_i, z_i)^T$. The following relationship is then represented by the homogeneous transformation:

$$\begin{pmatrix} \boldsymbol{p}_i \\ 1 \end{pmatrix} = \boldsymbol{T}(\boldsymbol{X}) \begin{pmatrix} \boldsymbol{p}_{Hi} \\ 1 \end{pmatrix} \qquad (1)$$

where $\boldsymbol{X} = (x, y, z, \phi, \theta, \psi)^T$. $(x, y, z)^T$ and $(\phi, \theta, \psi)^T$ are the 3D position and attitude angle (roll, pitch, and yaw angles), respectively, of the helmet in the world coordinate system. $\boldsymbol{T}(\boldsymbol{X})$ is the following homogeneous transformation matrix:

$$\boldsymbol{T}(\boldsymbol{X}) = \begin{pmatrix} \cos\theta\cos\psi & \sin\phi\sin\theta\cos\psi - \cos\phi\sin\psi & \cos\phi\sin\theta\cos\psi + \sin\phi\sin\psi & x \\ \cos\theta\sin\psi & \sin\phi\sin\theta\sin\psi + \cos\phi\cos\psi & \cos\phi\sin\theta\sin\psi - \sin\phi\cos\psi & y \\ -\sin\theta & \sin\phi\cos\theta & \cos\phi\cos\theta & z \\ 0 & 0 & 0 & 1 \end{pmatrix}$$

A voxel map with a cell size of 0.2 m per side is defined in the world coordinate system. In NDT scan matching, a normal distributions transformation is performed on the scan data obtained up to the previous time (referred to as reference scan data) in each cell of the voxel map, and the mean and covariance of the scan data in each cell are calculated.

The current self-pose $\boldsymbol{X}$ of the helmet is calculated by matching the scan data obtained at the current time (referred to as current scan data) with the reference scan data. The current scan data are mapped onto the world coordinate system by performing a coordinate transformation according to (1) using the pose $\boldsymbol{X}$. These data are then merged into the reference scan data. By repeating this process every LiDAR scan period, a LiDAR-based map is built.

B. Distortion Correction of LiDAR Scan Data

The helmet pose is determined every 100 ms (LiDAR scan period) by NDT scan matching. Scan data are acquired every 1.56 ms during one rotation of LiDAR. During LiDAR scanning, all scan data within one scan cannot be obtained at a single location when the micromobility is moving or swinging, or when the rider's body is swinging. If all scan data within one scan are transformed using the pose information of the helmet simultaneously, distortion appears in the mapping of the LiDAR scan data onto the world coordinate system. Therefore, the distortion in the scan data is corrected by estimating the helmet's pose using the EKF every 1.56 ms, i.e., every LiDAR scan data are obtained.

Figure 3 shows the sequence of distortion correction. The LiDAR scan period (100 ms) is denoted as τ, the IMU observation period (10 ms) as $\Delta\tau_{IMU}$, and the scan data observation period (1.56 ms) as $\Delta\tau$. Here, the method for correcting the distortion in scan data obtained between time $(t-1)\tau$ and $t\tau$ is described [15].

Let us suppose that at the time $(t-1)\tau$, the pose of the helmet is calculated by NDT scan matching and estimated using the EKF. IMU data are obtained 10 times per LiDAR scan ($\tau = 10\Delta\tau_{IMU}$). Using the IMU data obtained every $\Delta\tau_{IMU}$, the EKF estimates the pose $\hat{X}(t-1, k)$ at the time $(t-1)\tau + k\Delta\tau_{IMU}$, where $k = 0$–10. Because the observation period $\Delta\tau_{IMU}$ of the IMU is 10 ms, and the scan-data observation period $\Delta\tau$ is
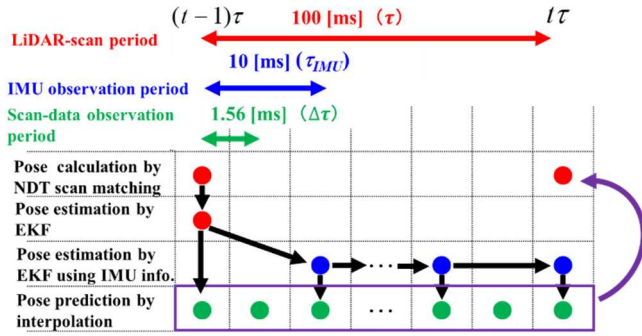
Figure 3. Sequence of distortion correction of LiDAR scan data.

1.56 ms, the LiDAR scan data are obtained six times within the IMU observation period ($\Delta\tau_{IMU} = 6\Delta\tau$).

From the estimates, $\hat{X}(t-1,k)$ at the time $(t-1)\tau + k\Delta\tau_{IMU}$ and $\hat{X}(t-1,k+1)$ at $(t-1)\tau + (k+1)\Delta\tau_{IMU}$, the interpolation algorithm predicts the helmet's pose $\hat{X}(t-1,k,j)$ at $(t-1)\tau + k\Delta\tau_{IMU} + j\Delta\tau$ (where $j = 1$–5), at which the scan data are acquired.

The scan data $p_{Hi}(t-1,k,j)$ (where $i = 1, 2, \ldots, n$) obtained at $(t-1)\tau + k\Delta\tau_{IMU} + j\Delta\tau$ in the helmet coordinate system are transformed into $p_i(t-1,k,j)$ in the world coordinate system using (1) as follows:

$$\begin{pmatrix} p_i(t-1,k,j) \\ 1 \end{pmatrix} = T(\hat{X}(t-1,k,j)) \begin{pmatrix} p_{Hi}(t-1,k,j) \\ 1 \end{pmatrix} \quad (2)$$

Using the pose estimate $\hat{X}(t-1,10)$ at $t\tau$ ($= (t-1)\tau + 10\Delta\tau_{IMU}$), the scan data $p_i(t-1,k,j)$ obtained by (2) is again transformed into the scan data $p_{Hi}^*(t)$ in the helmet coordinate system at $t\tau$ by

$$\begin{pmatrix} p_{Hi}^*(t) \\ 1 \end{pmatrix} = T(\hat{X}(t-1,10))^{-1} \begin{pmatrix} p_i(t-1,k,j) \\ 1 \end{pmatrix} \quad (3)$$

The $p_{Hi}^*(t)$ denotes the scan data corrected for distortion at $t\tau$. Using the corrected scan data, environmental map building and moving object tracking are performed. In the EKF for correcting scan data distortion, a constant velocity model is used as the helmet motion (see Appendix).
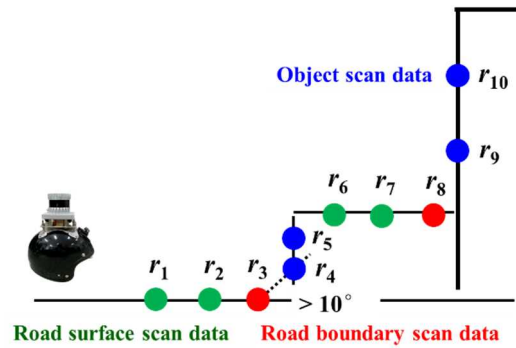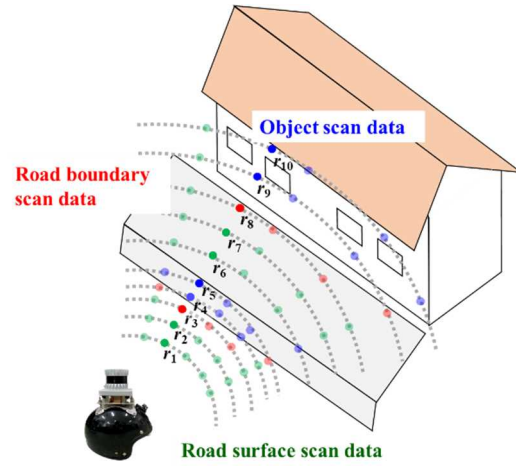
VI. CLASSIFICATION OF LiDAR SCAN DATA

The distortion-corrected LiDAR scan data are classified into scan data on road surfaces, road boundaries, and 3D objects using a rule-based method. Following that, the 3D object scan data are classified into stationary and moving object scan data using map subtraction (MS)-based classification and occupancy grid methods.
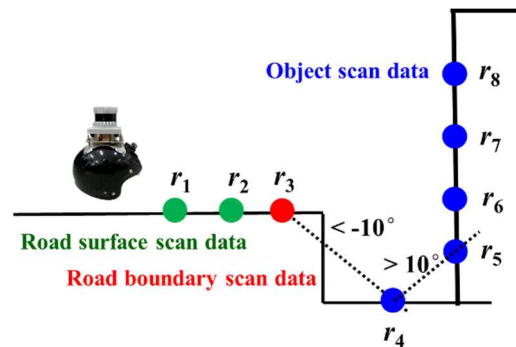
A. Classification of Road Surface, Road Boundary, and Object Scan Data

As shown in Figure 4 (a), 64 scan data points obtained for each 0.35° (vertical resolution) at a horizontal angle of the LiDAR laser beam, are arranged in order of decreasing elevation angle $r_1, r_2, r_3 \ldots$. First, we obtain the angle α of the line

connecting points r_1 and r_2 relative to the xy plane in the world coordinate system. If $|\alpha| \leq 10°$, r_2 is considered road surface scan data. This process is performed sequentially in other measurements $r_3, \ldots, r_n$. When $\alpha > 10°$, the scan data r_4, r_5, r_9, and r_{10} in Figure 4 (a) are considered convex object data. Then, the scan data r_3 and r_8 are considered the road boundary scan data. On the other hand, if $\alpha < -10°$, as r_4 in Figure 4 (b), the scan data are considered concave object data, and r_3 is considered road boundary scan data. This process is performed on all LiDAR scan data, and only the object scan data are used for subsequent processes.

(a) Convex obstacle

(b) Concave obstacle

Figure 4. Classification of LiDAR scan data. The green, red, and blue circles indicate scan data on road surfaces, road boundaries, and objects, respectively.

Because the boundary between the road surface and a 3D object can be obtained for fallen objects on the road, the method described above can recognize obstacles on the road.

The angle threshold to classify the scan data is set to 10°. If it is small, road slopes will be mis-detected as 3D objects. Generally, the slope of steep roads for vehicles is approximately 6°. Thus, a threshold value of 10°, which is larger than 6°, is set.

B. Classification of Stationary and Moving Object Scan Data

For map building, moving object scan data have to be eliminated, and stationary object scan data have to be extracted from the entire LiDAR scan data. Moving object tracking conversely requires the removal of stationary object scan data and the extraction of moving object scan data from the entire LiDAR scan data. For this, accurate classification of stationary and moving object scan data is required. Although, in our previous work [15], the classification was performed using the occupancy grid method, LiDAR noises and outliers frequently result in misclassification.

To mitigate the misclassification, we compare the current object scan data with stationary object scan data in a map built up to the previous time. We call this approach MS-based classification or dynamic background subtraction-based method [14]. Figure 5 shows the MS-based classification method. In this method, we subtract the stationary object scan data in the map from the current object scan data to remove as much stationary scan data as possible from the object scan data.

The scan data extracted using the MS-based method are mapped onto a grid map. The cell on the grid map is a square with a side length of 0.3 m. A cell with scan data is called an occupied cell. For the moving object scan data, the time to occupy the same cell is short (less than 0.8 s in this paper), whereas for the stationary object scan data, the time is long (not less than 0.8 s). Therefore, by using the occupancy grid method based on the cell occupancy time [28], cells occupied by moving object scan data (or stationary object scan data) can be detected as moving cells (or stationary cells).

Because an object can occupy multiple cells, adjacent occupied cells are clustered. Then, clustered moving cells (or stationary cells) are obtained as a moving cell group (or stationary cell group). The scan data contained in the moving cell group are finally determined as the moving object scan data. The stationary object scan data are extracted by subtracting the moving object scan data from the current object scan data.

The LiDAR field of view also moves along with the micromobility movement. Although an object that has recently entered the LiDAR field of view is stationary, it is misclassified as a moving object because the cell occupancy time is short. To address this problem, new-observation cells are defined on the grid map, which corresponds to the new LiDAR field of view. The time of cells entering the LiDAR field of view (T_{NC}) and the cell occupancy time (T_{OC}) are measured, and the occupancy time rate (β) is calculated by $\beta = T_{OC} / T_{NC}$. Cells with β of 10% or more are determined to be new-observation cells and then considered moving cells. This can minimize the false classification of stationary objects that recently entered the LiDAR field of view as moving objects.

The scan data in the map are sparser in the areas in front of the micromobility and the occlusion areas. Therefore, the stationary object scan data likewise exist in a sparse state when
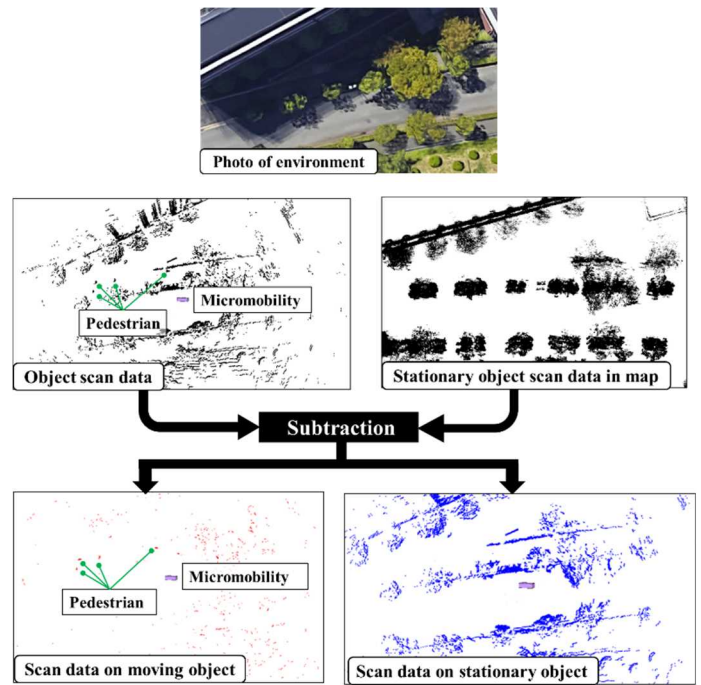

Figure 5. Sequence of MS-based classification (top view).

the map is subtracted from the current object scan data. If the scan data, sparsely extracted using the MS-based method, are mapped onto a grid map, they may be erroneously determined as moving cells.

To overcome this issue, the scan data removed using the MS-based method are also mapped onto the grid map as stationary cells. As a result, sparse stationary object scan data that tend to be moving cells and stationary object scan data removed by the MS-based method are both mapped onto the grid map. The neighboring cells, which these stationary object scan data occupy, are clustered, and the cell group is then determined to be a stationary cell group. Accordingly, sparse stationary object scan data are correctly determined as stationary object scan data using the occupancy grid method.

In our preliminary experiments, LiDAR could correctly detect objects located within a range of approximately 50 m from the helmet. A grid map is therefore set up in ±35 m squares from the helmet; the distance from the helmet to the vertex of the square is approximately 50 m. Considering the resolution (0.35°) of the horizontal viewing angle of LiDAR, the cell size of the grid map is set to 0.3 m so that at least one measurement of LiDAR could be occupied in a cell 50 m away from the helmet. Assuming that the width and length of a pedestrian are 0.4 m and the walking speed is greater than 1 m/s, the time that the LiDAR measurements related to the pedestrian occupying a cell is less than 0.8 s. Therefore, the threshold of the occupation time to determine stationary and moving cells is set to 0.8 s.

VII. Road Boundary Estimation and Moving Object Tracking

In this section, the methods for estimating road boundaries and tracking moving objects are described using road boundary and moving object scan data, respectively.

A. Road Boundary Estimation

Although large boundaries between motor roads and sidewalks, such as grooves and curbs, can be detected every LiDAR scan period (100 ms), misdetection due to sensor errors and disturbances frequently occurs. Therefore, detection accuracy for road boundaries is improved using the following method. A grid map is created with the helmet position in the *xy*-plane in the world coordinate system as its center. Here, the cell on the grid map is a square with a side length of 0.5 m. Road boundary scan data obtained every LiDAR scan period (100 ms) are mapped onto the cell (referred to as road boundary cell) of the grid map.

The occupancy time (R_{OC}) is measured when road boundary scan data occupy each road boundary cell, and the unoccupied time (R_{UOC}) is also measured when they are unoccupied. If the total time ($R_{OC} + R_{UOC}$) is greater than 2 s and the ratio of occupation time to the total time, $R_{OC}/(R_{OC} + R_{UOC})$ is greater than 70 %, the scan data in the road boundary cell are considered road boundary scan data.

Because the width of grooves is generally 0.3–0.5 m, the size of the boundary cell is set to 0.5 m.

B. Moving Object Tracking [29]

In moving object tracking, the shape of the moving object is represented by a cuboid with a width W, a length L, and a height H, as depicted in Figure 6. The width W_{meas} and length L_{meas} of the moving object are extracted from the moving object scan data. With these values, W and L of the moving object are estimated by

$$\begin{cases} W(t) = W(t-1) + G(W_{meas} - W(t-1)) \\ L(t) = L(t-1) + G(L_{meas} - L(t-1)) \end{cases} \quad (4)$$

where G represents the gain.

The height estimate H of the moving object is obtained from the height measurements of the moving object scan data.

The Kalman filter is used to estimate the position and velocity of the moving object in the world coordinate system based on the centroid position of the rectangle estimated from (4). In crowded environments, the rule-based data association method is used to accurately match multiple moving objects with multiple moving scan data.

For the Kalman-filter-based tracking of moving object, it is assumed that the object moves at an approximately constant velocity. The motion model of the object is then given by

$$\boldsymbol{x}(t) = \begin{pmatrix} 1 & \tau & 0 & 0 \\ 0 & 1 & 0 & 0 \\ 0 & 0 & 1 & \tau \\ 0 & 0 & 0 & 1 \end{pmatrix} \boldsymbol{x}(t-1) + \begin{pmatrix} \tau^2/2 & 0 \\ \tau & 0 \\ 0 & \tau^2/2 \\ 0 & \tau \end{pmatrix} \varDelta \boldsymbol{x}(t-1) \quad (5)$$

where $\boldsymbol{x} = (x, \dot{x}, y, \dot{y})^T$. $(x, y)^T$ and $(\dot{x}, \dot{y})^T$ are the position and velocity, respectively. $\varDelta \boldsymbol{x} = (\varDelta \ddot{x}, \varDelta \ddot{y})^T$ is an unknown acceleration (plant noise).

If the object moves with various different motions, such as moving at a constant speed, going or stopping suddenly, or turning suddenly, the use of multi-model-based tracking, such
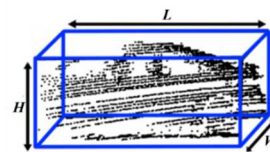

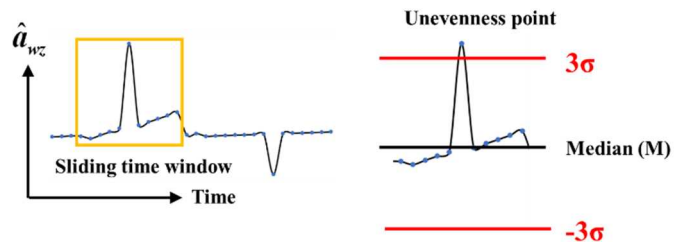Figure 6. Cuboid around the tracked object (car).

Figure 7. Threshold for road unevenness detection.

as an interacting-multiple-model estimator [30], will improve the tracking performance.

VIII. DETECTION OF ROAD UNEVENNESS AND ESTIMATION OF ROAD SURFACE CONDITION

In this section, the methods for detecting small road unevenness and estimating road surface conditions with acceleration data from IMU are described. The related information can be used to prevent falling risks of micromobility and to improve rider comfort.

A. Detection of Small Road Unevenness

Because it is difficult to detect small unevenness on roads with LiDAR, such as dents, cracks, and manhole covers, they are detected using IMU data. The acceleration obtained from the IMU in the helmet coordinate system is denoted by $\boldsymbol{a}_H = (a_{Hx}, a_{Hy}, a_{Hz})^T$. Because the acceleration data include the gravitational acceleration G, the acceleration $\hat{\boldsymbol{a}}_H$, where the gravitational acceleration is removed, is given by

$$\hat{\boldsymbol{a}}_H = \boldsymbol{a}_H - G \begin{pmatrix} -\sin\theta \\ \sin\phi\cos\theta \\ \cos\phi\cos\theta \end{pmatrix} \quad (6)$$

where ϕ and θ represent the roll and pitch angles, respectively, of the helmet obtained from the IMU in the world coordinate system.

Then, the acceleration $\hat{\boldsymbol{a}}_W = (\hat{a}_{Wx}, \hat{a}_{Wy}, \hat{a}_{Wz})^T$ in the world coordinate system is given by

$$\hat{\boldsymbol{a}}_W = \begin{pmatrix} \cos\theta & \sin\phi\sin\theta & \cos\phi\sin\theta \\ 0 & \cos\phi & -\sin\phi \\ -\sin\theta & \sin\phi\cos\theta & \cos\phi\cos\theta \end{pmatrix} \hat{\boldsymbol{a}}_H \quad (7)$$

When $|\hat{a}_{Wz}|$ exceeds a threshold, it is assumed that the micromobility encounters small road unevenness. The threshold of unevenness detection is determined using a Hampel filter [31]. As shown in Figure 7, the acceleration data

$\hat{a}_{wz}$ are separated by a sliding-time window (window size of 5 s in this paper), and median (M) and standard deviation (σ) are calculated for the acceleration data in this window. From the calculation, the points $\hat{a}_{wz} \leq M - 3\sigma$ or $\hat{a}_{wz} \geq M + 3\sigma$ are detected as road unevenness.

The locations of road unevenness in the world coordinate systems are determined based on the self-pose of the helmet.

B. Estimation of Road Surface Condition

Micromobilities travel on various roads, including non-paved roads, such as gravel roads, and paved roads that are not suitably maintained. Because the road surface condition is closely related to the safety of the micromobility, as well as rider comfort, it is also estimated from acceleration data to build a related map.

The International Roughness Index (IRI) [32] is used as an evaluation index for road surface conditions. To obtain IRI values, the vertical displacement caused by road unevenness, is calculated by integrating the acceleration data $\hat{a}_{wz}$. Because of the low-frequency noise of acceleration data, double integration of acceleration data with respect to time significantly leads to drift errors in the estimation of the vertical displacement.

To accurately obtain the vertical displacement, the acceleration data are integrated in the frequency domain, as follows. First, the acceleration data are passed through a Hanning window to remove sidelobes, and Fourier transform is performed. Following this, low-frequency noise is removed using a high-pass filter, and double integration is performed. The vertical displacement is then obtained by inverse Fourier transform.

The vertical displacement calculated from the acceleration data, which is obtained every IMU observation period (10 ms), is denoted by d_i. Then, the IRI value, J, for every S (10 m in this paper) of the traveled distance of the helmet is given by

$$J = \frac{1}{S} \sum_{i=1}^{n} |d_i| \qquad (8)$$

where S is obtained from the self-pose of the helmet.

Note that the units of d_i, S, and J are mm, m, and mm/m, respectively. The higher the IRI value J, the rougher the road surface condition.

Because the IMU is mounted on the helmet, the head motion of the rider may affect the estimation of the vertical displacement. To reduce the effect of the rider's head motion as well as the low-frequency noise of acceleration data, the cut-off frequency of the high-pass filter is set to 10 Hz.

IX. FUNDAMENTAL EXPERIMENTS

In this section, the performance of our method is evaluated through experiments in a road environment on our university campus.

A. Results of Map Building and Moving Object Tracking

A micromobility was moved on our university campus road, as shown in Figure 8, and environmental map building and moving object tracking with LiDAR scan data were performed. The traveled distance of micromobility is approximately 500 m, and the maximum speed is approximately 30 km/h. Figure 9 shows the attitude angle and angular velocity of the helmet during movement, which are observed by the IMU.

The experiments are conducted in the following two cases:
- Case 1: Map building and moving object tracking with the distortion correction of LiDAR scan data and the MS-based classification method (the proposed method)
- Case 2: Map building and moving object tracking without using either method.
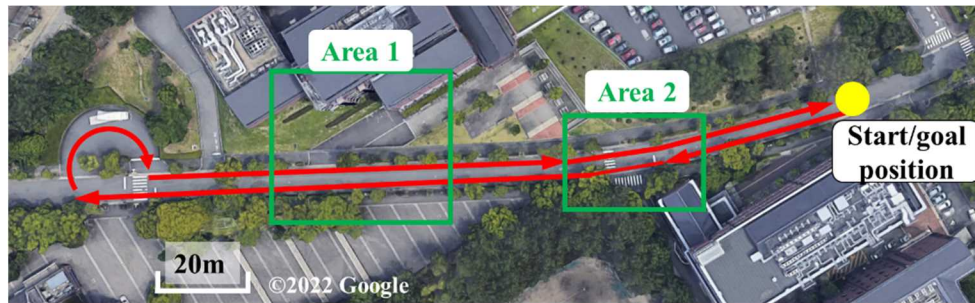
(a) Top view

(b) Side view

(c) Curbstone. The longitudinal offset from road is 150 mm.

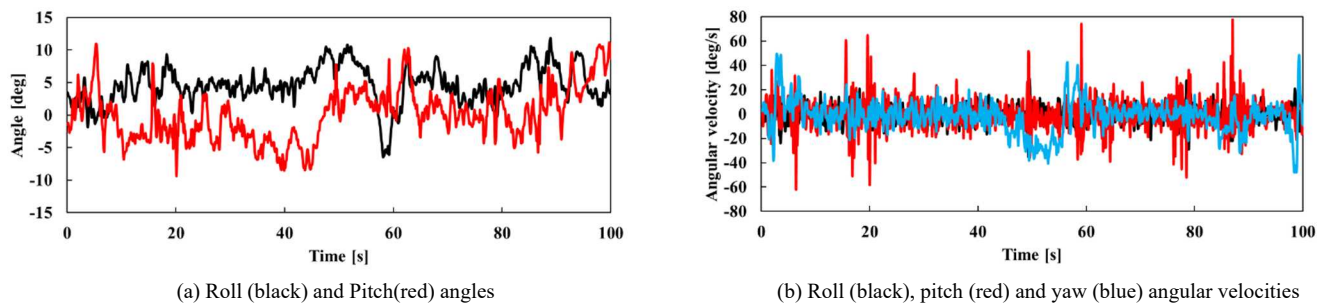Figure 8. Photo of experimental environment.

(a) Roll (black) and Pitch(red) angles

(b) Roll (black), pitch (red) and yaw (blue) angular velocities

Figure 9. Attitude angle and angular velocity of helmet.

(a) Overall map (top view)

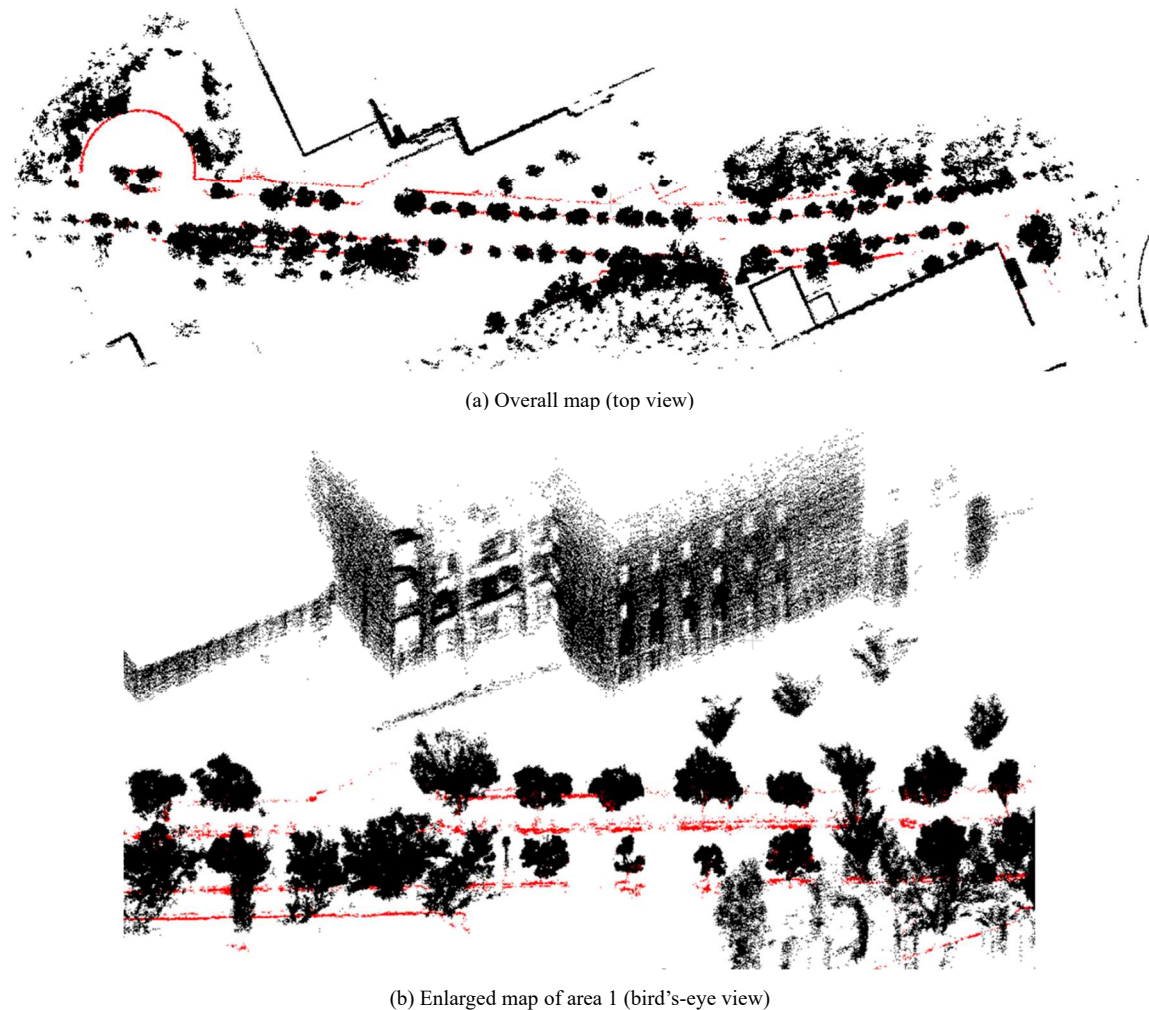(b) Enlarged map of area 1 (bird's-eye view)

Figure 10. Map-building result. The black dots indicate stationary object scan data, and the red dots indicate estimated road boundaries.

In case 2, although the distortion of LiDAR scan data is not corrected, the self-pose of the helmet is estimated using the EKF.

Figure 10 shows the result of map building obtained using the proposed method (case 1). This figure shows that the proposed method can build an environmental map.

In our SLAM-based-map building method, the accuracy of map building is equivalent to that of the self-pose estimate of a helmet. Therefore, to evaluate the accuracy of map building, the error of position estimate of the helmet at the goal position is measured using a GNSS/LiDAR positioning system set at the goal position. Table I shows the result, where the micromobility is moved thrice on the road shown in Figure 8. According to the table, the proposed method (case 1) provides better map-building accuracy than case 2.
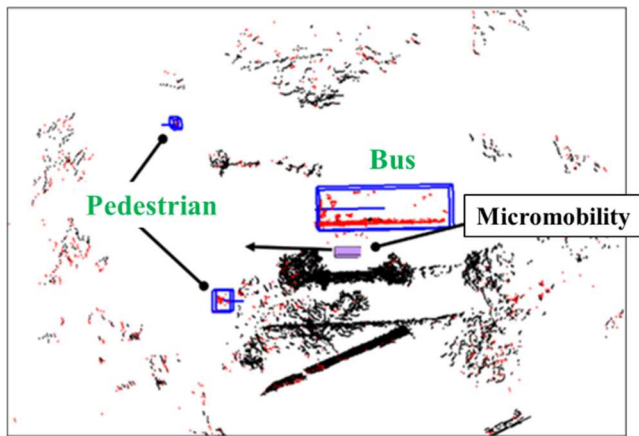
Figure 11 presents the result of moving object tracking in area 2 shown in Figure 8. In (b), the blue rectangle indicates the assessed size of the moving object, and the blue stick indicates

TABLE I. ERROR IN POSITION ESTIMATE OF HELMET AT GOAL POSITION.

	Experiment 1	Experiment 2	Experiment 3
Case 1	0.38 m	1.98 m	0.68 m
Case2	5.91 m	15.10 m	6.03 m

(a) Photo of area 2

(b) Estimated position and size of moving objects in area 2

Figure 11. Result of moving object tracking (top view).

the moving direction of the moving object obtained from the velocity estimate. The black (or red) dots indicate the scan data removed (or extracted) from the LiDAR scan data using the MS-based method.

In experiments 1–3, there are 111 moving objects (106 pedestrians and five cars). As a result, in case 1 (proposed method), 109 objects (104 pedestrians and five cars) can be successfully tracked, and two pedestrians cannot be tracked. Conversely, in case 2, 103 objects (98 pedestrians and five cars) can be successfully tracked, and eight pedestrians cannot be tracked. From these results, our proposed method achieves better accuracy in moving object tracking.

Pedestrians who are not being tracked walk close to trees. In case 2, moving cells related to pedestrians are merged with adjacent stationary cells related to trees using the occupancy grid method, and pedestrians are falsely detected as stationary objects. On the other hand, because, in case 1, the stationary cells related to trees are removed using the MS-based classification method, pedestrians are detected correctly. Consequently, untracking of pedestrians occurs more often in case 2 than in case 1.

B. Results of Detection of Road Unevenness and Estimation of Road Surface Condition

A micromobility was moved on an asphalt-paved road on our university campus, as depicted in Figure 12. Four unevenness (three curbs and a crack) on the road shown in Figure 12 are detected, and road roughness condition is estimated. It is expected that the accuracy of detecting road unevenness and estimating road surface conditions is affected by rider weight, vehicle speed, vehicle dynamics, and so on. Therefore, the experiments are conducted under conditions of different rider weights (55, 65, and 76 kg) and micromobility velocities (10 and 15 km/h).

Figure 13 shows the vertical acceleration $\hat{a}_{vz}$ calculated from IMU data obtained while driving of the micromobility. Table II shows the success rate of detecting road unevenness. From the results, when the rider weight is light, the vertical acceleration to road unevenness becomes small, and the success rate of detection decreases.
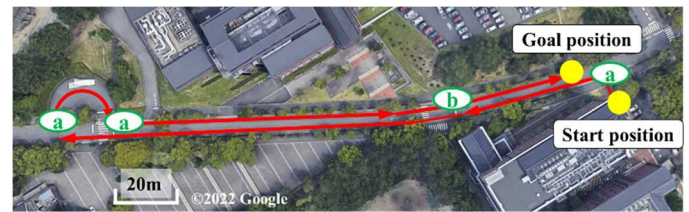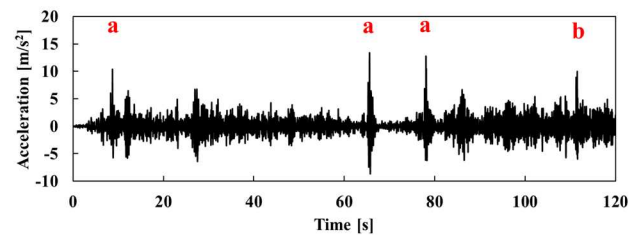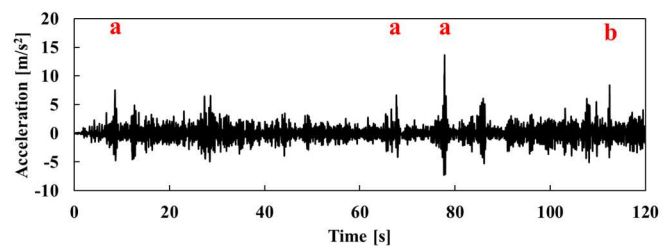

a) Curb (+-15mm)

b) Crack (-6mm)

Figure 12. Moved path of micromobility, and curb (a) and crack (b) on road. Numerals indicate the longitudinal offsets of the road unevenness.

(a) Rider weight of 75 kg, and micromobility velocity of 15 km/h

(b) Rider weight of 55 kg, and micromobility velocity of 15 km/h

Figure 13. Vertical acceleration. The "a" and "b" mean the times when the micromobility encounters on curb and crack, respectively, shown in Figure 12.

TABLE II. SUCCESS RATE OF ROAD UNEVENNESS DETECTION

		Road Unevenness	
		a: curb	*b: crack*
Rider Weight	*55 kg*	44.4 % (4/9)	66.7 % (2/3)
	65 kg	83.3 % (10/12)	100 % (4/4)
	75 kg	100 % (9/9)	66.7 % (2/3)
Total		76.7 % (23/30)	80.0 % (8/10)

*The "c" and "d" in c/d indicate the number of detected unevenness and the number of times when the micromobility encounters the unevenness, respectively.

Next, as shown in Figure 14, the path traveled by the micromobility is divided into 79 sections of 10 m each, and the IRI values are obtained, where the road unevenness (curb and crack) shown in Figure 12 are in sections 4, 44, 50, and 75. Figure 15 (a) shows the results. Because the IRI values for the rider with a weight of 55 kg are small and lead to inaccuracy, the mean of the IRI values for riders with weights of 65 and 75 kg is calculated. The mean is shown in Figure 15 (b). Figure 16 shows a map of the road surface condition, which is drawn based on the mean of the IRI values in Figure 15 (b).
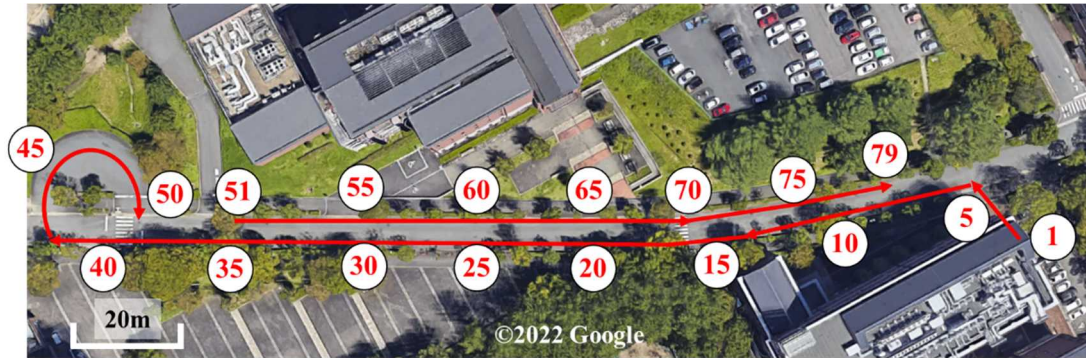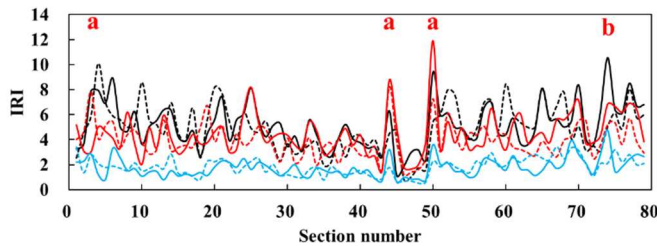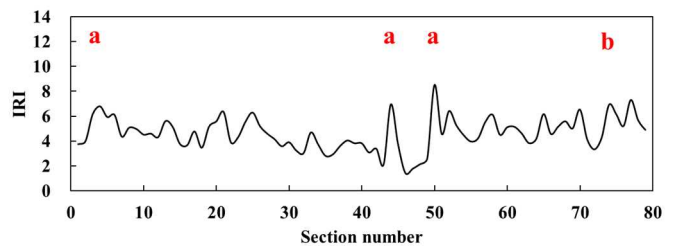

Figure 14. Section for IRI value estimation.

(a) IRI value by different rider weights and micromobility velocities

(b) Mean of IRI value

Figure 15. Estimation result of road surface conditions. In (a), black solid line (weight of 75 kg and velocity of 15 km/h), black dashed line (75 kg and 10 km/h), red solid line (65 kg and 15 km/h), red dashed line (65 kg and 10 km/h), light blue solid line (55 kg and 15 km/h), and light blue dashed line (55 kg and 10 km/h).
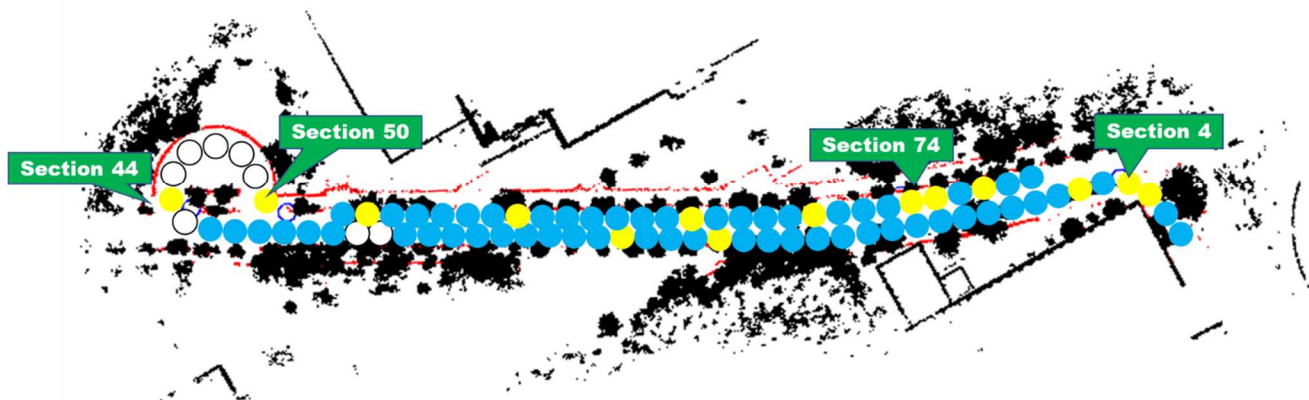

Figure 16. Map of road surface conditions. Different colored circles indicate IRI levels (white:0–3 mm/m, light blue: 3–6, and yellow:6–9).

| (a) Section 25 (6.28 mm/m) | (b) Section 52 (6.40 mm/m) | (c) Section 70 (6.52 mm/m) | (d) Section 77 (7.29 mm/m) |

| (e) Section 13 (5.59 mm/m) | (f) Section 49 (2.57 mm/m) | (g) Section 61 (5.13 mm/m) | (h) Section 66 (4.56 mm/m) |

Figure 17. Photo of road surfaces in eight sections. Numerals in brackets indicate the estimated IRI values. The IRI level of (a)–(d) is high (yellow circle in Figure 16), and that of (e)–(h) is low (white and light blue circles in Figure 16).

Because most of the sections on which the micromobility travels are flat asphalt-paved roads, the IRI values are small in most sections. Figure 17 shows the photos of road surfaces and the estimated IRI values in eight of 79 sections. The IRI values in sections 4, 44, 50, and 74, where there is road unevenness (curb and crack), as shown in Figure 12, are 6.78, 6.94, 8.49, and 6.90, respectively.

Because we currently do not have any professional instruments to accurately measure IRI values on roads, such as a car-mounted laser pavement scanner, the true IRI value is unknown, and the performance of our road surface condition estimation cannot be evaluated quantitatively.

The root mean square (RMS) values of the IRI values shown in Figure 15 (a) are 5.48 mm/m (rider weight of 75 kg and micromobility velocity of 15 km/h), 5.30 mm/m (75 kg and 10 km/h), 4.77 mm/m (65 kg and 15 km/h), 4.13 mm/m (65 kg and 10 km/h), 1.93 mm/m (55 kg and 15 km/h), and 1.98 mm/m (55 kg and 10 km/h). These RMS values and Table II show that the accuracy of the road surface condition map built using acceleration data is affected by rider weight and micromobility velocity. Eliminating those effects and improving map accuracy could be performed using a machine learning-based method, where the results of road unevenness detection and road surface condition estimation are collected from many micromobilities traveling on the same road. A related study in this regard is one of our future works.

The building of maps related to stationary objects, road boundaries, and road unevenness, as well as tracking of moving objects, should be performed in real time after each LiDAR scan data and IMU acceleration data are obtained. In our experiments, LiDAR scan data and IMU data are recorded, and map building and moving object tracking are performed offline using a computer. The specifications of the computer are as follows: Windows 10 Pro OS, Intel(R) Core (TM) i7-1065G7 @1.30GHz CPU, 16 GB RAM, and C++ software language. The point cloud library [33] is used for NDT scan matching.

The RMS values of the processing times are as follows:
- Distortion correction and NDT scan matching: 4048 ms
- Classification of LiDAR scan data: 2153 ms
- Map update of stationary objects and road boundaries: 39 ms
- Moving object tracking: 247 ms
- Detection of road unevenness: 3 ms
- Total: 6317 ms

Although a long computational time is currently required for map building and moving object tracking, the computational time can be reduced by optimizing the program code and using a graphical processing unit for real-time operations.

X. CONCLUSION AND FUTURE WORK

This paper presented a method of experimental map building and moving object tracking using LiDAR and IMU attached to a helmet worn by a rider of micromobility. To accurately perform LiDAR-based environmental mapping and moving object tracking, the distortion of scanning LiDAR data was corrected using the self-pose information by NDT scan matching and IMU information using the EKF.

The distortion-corrected LiDAR scan data were classified into different data types to build a map composed of scan data relating to stationary objects and road boundaries and to track moving objects. Furthermore, road unevenness was detected, and road surface conditions were estimated using acceleration information from the IMU, and the related map was built to reduce the falling risk of micromobility and to provide comfort

of the rider. The performance of the presented method was examined through experiments in a road environment on our university campus.

In future works, experiments in various sidewalk and roadway environments will be conducted to thoroughly evaluate the proposed method. The accuracy of the environmental map will be improved by collecting and processing map information obtained from many micromobilities. In addition, the realization of environment map building and moving object tracking using small and lightweight solid-state LiDAR instead of the mechanical LiDAR used in this paper is an important future direction.

APPENDIX: MOTION MODEL OF HELMET

As shown in Figure A, the translational velocity of the helmet in the helmet coordinate system (O_H-$x_Hy_Hz_H$) is denoted by (V_x,V_y,V_z), and the angular velocity (roll, pitch, and yaw angular velocities) by ($\dot{\phi}_H,\dot{\theta}_H,\dot{\psi}_H$).

The following motion model of the helmet can be obtained assuming that the helmet moves at nearly constant translational and rotational velocities:

$$
\begin{pmatrix} x_{(t+1)} \\ y_{(t+1)} \\ z_{(t+1)} \\ \phi_{(t+1)} \\ \theta_{(t+1)} \\ \psi_{(t+1)} \\ V_{x(t+1)} \\ V_{y(t+1)} \\ V_{z(t+1)} \\ \dot{\phi}_{H(t+1)} \\ \dot{\theta}_{H(t+1)} \\ \dot{\psi}_{H(t+1)} \end{pmatrix} =
\begin{pmatrix}
\begin{aligned} & x_{(t)} + a_{1(t)}\cos\theta_{(t)}\cos\psi_{(t)} \\ & + a_{2(t)}\{\sin\phi_{(t)}\sin\theta_{(t)}\cos\psi_{(t)} - \cos\phi_{(t)}\sin\psi_{(t)}\} \\ & + a_{3(t)}\{\cos\phi_{(t)}\sin\theta_{(t)}\cos\psi_{(t)} + \sin\phi_{(t)}\sin\psi_{(t)}\} \end{aligned} \\
\begin{aligned} & y_{(t)} + a_{1(t)}\cos\theta_{(t)}\sin\psi_{(t)} \\ & + a_{2(t)}\{\sin\phi_{(t)}\sin\theta_{(t)}\sin\psi_{(t)} + \cos\phi_{(t)}\cos\psi_{(t)}\} \\ & + a_{3(t)}\{\cos\phi_{(t)}\sin\theta_{(t)}\sin\psi_{(t)} - \sin\phi_{(t)}\cos\psi_{(t)}\} \end{aligned} \\
\begin{aligned} & z_{(t)} - a_{1(t)}\sin\theta_{(t)} + a_{2(t)}\sin\phi_{(t)}\cos\theta_{(t)} \\ & + a_{3(t)}\cos\phi_{(t)}\cos\theta_{(t)} \end{aligned} \\
\phi_{(t)} + a_{4(t)} + \{a_{5(t)}\sin\phi_{(t)} + a_{6(t)}\cos\phi_{(t)}\}\tan\theta_{(t)} \\
\theta_{(t)} + \{a_{5(t)}\cos\phi_{(t)} - a_{6(t)}\sin\phi_{(t)}\} \\
\psi_{(t)} + \{a_{5(t)}\sin\phi_{(t)} + a_{6(t)}\cos\phi_{(t)}\}\dfrac{1}{\cos\theta_{(t)}} \\
V_{x(t)} + \tau w_{\dot{V}x} \\
V_{y(t)} + \tau w_{\dot{V}y} \\
V_{z(t)} + \tau w_{\dot{V}z} \\
\dot{\phi}_{H(t)} + \tau w_{\ddot{\phi}_H} \\
\dot{\theta}_{H(t)} + \tau w_{\ddot{\theta}_H} \\
\dot{\psi}_{H(t)} + \tau w_{\ddot{\psi}_H}
\end{pmatrix}
$$

(A)

where (x,y,z) and (ϕ,θ,ψ) denote the position and attitude angle (roll, pitch, and yaw angles), respectively, of the helmet in the world coordinate system (O_w-$x_wy_wz_w$). ($w_{\dot{V}x},w_{\dot{V}y},w_{\dot{V}z},w_{\ddot{\phi}_H},w_{\ddot{\theta}_H},w_{\ddot{\psi}_H}$) denotes the acceleration disturbance. τ denotes the sampling period of LiDAR scan data and IMU data. $a_1=V_x\tau+\tau^2 w_{\dot{V}x}/2$, $a_2=V_y\tau+\tau^2 w_{\dot{V}y}/2$, $a_3=V_z\tau+\tau^2 w_{\dot{V}z}/2$, $a_4=\dot{\phi}_H\tau+\tau^2 w_{\ddot{\phi}_H}/2$, $a_5=\dot{\theta}_H\tau+\tau^2 w_{\ddot{\theta}_H}/2$, and $a_6=\dot{\psi}_H\tau+\tau^2 w_{\ddot{\psi}_H}/2$.
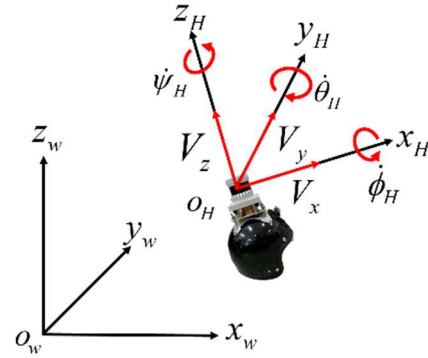

Figure A. Notation for helmet motion.

REFERENCES

[1] I. Yoshida, A. Yoshida, M. Hashimoto, and K. Takahashi, "Simultaneous Localization, Mapping and Moving-Object Tracking Using Helmet-Mounted LiDAR for Micromobility," Proc. the 13th Int. Conf. on Sensor Device Technologies and Applications, pp. 25–31, 2022.

[2] E. Yurtsever, J. Lambert, A. Carballo, and K. Takeda, "A Survey of Autonomous Driving: Common Practices and Emerging Technologies," IEEE Access, vol. 8, pp. 58443–58469, 2020.

[3] V. Balaska et al., "A Viewpoint on the Challenges and Solutions for Driverless Last-Mile Delivery," Machines 2022, 10, 1059, 2022.

[4] B. Huang, J. Zhao, and J. Liu, "A Survey of Simultaneous Localization and Mapping," eprint arXiv:1909.05214, 2019.

[5] S. Kuutti et al., "A Survey of the State-of-the-Art Localization Techniques and Their Potentials for Autonomous Vehicle Applications," IEEE Internet of Things Journal, vol.5, pp. 829–846, 2018.

[6] A. Mukhtar, L. Xia, and TB. Tang, "Vehicle Detection Techniques for Collision Avoidance Systems: A Review," IEEE Trans. Intelligent Transportation Systems, vol. 16, pp. 2318–2338, 2015.

[7] Á. Llamazares, E. J. Molinos, and M. Ocaña, "Detection and Tracking of Moving Obstacles (DATMO): A Review," Robotica, vol. 38, pp. 761–774, 2020.

[8] E. Marti, J. Perez, MA. Miguel, and F. Garcia, "A Review of Sensor Technologies for Perception in Automated Driving," IEEE Intelligent Transportation Systems Magazine, pp. 94–108, 2019.

[9] Q. Chena, Y. Xiea, S. Guob, J. Baic, and Q. ShudaKey, "Sensing System of Environmental Perception Technologies for Driverless Vehicle: A Review of State of the Art and Challenges," Sensors and Actuators A: Physical, vol. 319, 112566, 2021.

[10] B. Sengul and H. Mostofi, "Impact of E-Micromobility on the Sustainability of Urban Transportation-A Systematic Review," Applied Science. 2021, 11(13), 5851, 2021.

[11] S. Tanaka, C. Koshiro, M. Yamaji, M. Hashimoto, and K. Takahashi, "Point Cloud Mapping and Merging in GNSS-Denied and Dynamic Environments Using Only Onboard Scanning LiDAR," Int. J. Advances in Systems and Measurements, vol. 13, pp. 275–288, 2020.

[12] K. Matsuo, A. Yoshida, M. Hashimoto, and K. Takahashi, "NDT Based Mapping Using Scanning Lidar Mounted on Motorcycle,"

Proc. the Fifth Int. Conf. on Advances in Sensors, Actuators, Metering and Sensing, pp. 69–75, 2020.

[13] S. Sato, M. Hashimoto, M. Takita, K. Takagi, and T. Ogawa, "Multilayer Lidar-Based Pedestrian Tracking in Urban Environments," Proc. IEEE Intelligent Vehicles Symp., pp. 849–854, 2010.

[14] S. Muro, I. Yoshida, M. Hashimoto, and K. Takahashi, "Moving-Object Tracking by Scanning LiDAR Mounted on Motorcycle Based on Dynamic Background Subtraction," Artificial Life and Robotics, vol. 26, issue 4, pp. 412–422, 2021.

[15] I. Yoshida, A. Yoshida, M. Hashimoto, and K. Takahashi, "Map Building Using Helmet-Mounted LiDAR for Micro-Mobility," Artificial Life and Robotics, vol. 28, issue 2, pp. 471–482, 2023.

[16] Y. Cai, S. Hackett, G., Ben, F. Alber, and S. Mel, "Heads-Up Lidar Imaging with Sensor Fusion," Electronic Imaging, The Engineering Reality of Virtual Reality 2020, pp. 338-1–338-7, 2020.

[17] B. Cinaz and H. Kenn, "Head SLAM- Simultaneous Localization and Mapping with Head-Mounted Inertial and Laser Range Sensors," Proc. 12th IEEE Int. Symp. on Wearable Computers, 2008.

[18] H. Sadruddin, A. Mahmoud, and M. M. Atia, "Enhancing Body-Mounted LiDAR SLAM using an IMU-based Pedestrian Dead Reckoning (PDR) Model," Proc. 2020 IEEE 63rd Int. Midwest Symp. on Circuits and Systems, 2020.

[19] E. Niforatos, I. Elhart, A. Fedosov, and M. Langheinrich, " s-Helmet: A Ski Helmet for Augmenting Peripheral Perception," Proc. the 7th Augmented Human Int. Conf.,2016.

[20] K. Zang, J. Shen, H. Huang, M. Wan, and J. Shi, "Assessing and Mapping of Road Surface Roughness based on GPS and Accelerometer Sensors on Bicycle-mounted Smartphones," Sensors, 2018, 18, 914, 2018.

[21] S. Cafiso, A. D. Graziano, V. Marchetta, and G. Pappalardo, "Urban Road Pavements Monitoring and Assessment Using Bike and E-scooter as Probe Vehicles," Case Studies in Construction Materials 16, 2022.

[22] K. R. Opara, K. Brzezinski, M. Bukowicki, and K. Kaczmarek-Majer, "Road Roughness Estimation Through Smartphone-Measured Acceleration," IEEE Intelligent Transportation Systems Magazine, pp. 209–220, 2022.

[23] W. Titov and T. Schlegel, "Monitoring Road Surface Conditions for Bicycles – Using Mobile Device Sensor Data from Crowd Sourcing," HCI in Mobility, Transport, and Automotive Systems, pp. 340–356, 2019.

[24] V. Douangphachanh and H. Oneyama, "Formulation of a Simple Model to Estimate Road Surface Roughness Condition from Android Smartphone Sensors," Proc. 2014 IEEE Ninth Int. Conf. on Intelligent Sensors, Sensor Networks and Information, 2014.

[25] A. Pangestu, M. N. Mohammed, S. Al-Zubaidi, S. H. K. Bahrain, and A. Jaenul, "An Internet of Things Toward a Novel Smart Helmet for Motorcycle: Review," AIP Conf. Proceedings 2320, 050026, 2021.

[26] T. Raj, F. H. Hashim, A. B. Huddin, M. F. Ibrahim, and A. Hussain, "A Survey on LiDAR Scanning Mechanisms," Electronics, vol. 9, 2020.

[27] P. Biber and W. Strasser, "The Normal Distributions Transform: A New Approach to Laser Scan Matching," Proc. IEEE/RSJ Int. Conf. on Intelligent Robots and Systems, pp. 2743–2748, 2003.

[28] M. Hashimoto, S. Ogata, F. Oba, and T. Murayama, "A Laser Based Multi-Target Tracking for Mobile Robot," Intelligent Autonomous Systems 9, pp. 135–144, 2006.

[29] Y. Tamura, R. Murabayashi, M. Hashimoto, and K. Takahashi, "Hierarchical Cooperative Tracking of Vehicles and People Using Laser Scanners Mounted on Multiple Mobile Robots," Int. J. Advances in Intelligent Systems, vol. 10, no. 1 & 2, pp. 90–101, 2017.

[30] E. Mazor, A. Averbuch, Y. Bar-Shalom, and J. Dayan, "Interacting Multiple Model Methods in Target Tracking: A Survey," IEEE Trans. Aerospace and Electronic Systems, vol.34, pp.103–123, 1998.

[31] R. Wicklin, "The Hampel Identifier: Robust Outlier Detection in a Time Series," https://blogs.sas.com/content/iml/2021/06/01/hampel-filter-robust-outliers.html, 10 September, 2022.

[32] O. G. Dela Cruz, C. A. Mendoza, and K. D. Lopez, "International Roughness Index as Road Performance Indicator: A Literature Review," IOP Conf. Series: Earth and Environmental Science, vol. 822, 2021.

[33] R. B. Rusu and S. Cousins, "3D is here: Point Cloud Library (PCL)," Proc. 2011 IEEE Int. Conf. on Robotics and Automation, 2011.